Bottom Up Synthesis of Boron-Doped Graphene for Stable Intermediate Temperature Fuel Cell Electrodes

[#]Wesley D. Tennyson[a], [#]Mengkun Tian[b], Alexander B. Papandrew[b], Christopher M. Rouleau[a], Alexander A. Puretzky[a], Brian T. Sneed[a], Karren L. More[a], Gabriel M. Veith[c], Gerd Duscher,[c,d] Thomas A. Zawodzinski[c,d], *David B. Geohegan[a]

[a] *Center for Nanophase Materials Sciences, Oak Ridge National Laboratory, Oak Ridge, TN, 37831 USA*

[b] *Department of Chemical and Biomolecular Engineering, University of Tennessee, Knoxville, TN 37996 USA*

[c] *Materials Science and Technology Division, Oak Ridge National Laboratory, Oak Ridge, TN 37831 USA*

[d] *Department of Materials Science and Engineering, University of Tennessee, Knoxville, TN 37996 USA*

Notice: This manuscript has been authored by UT-Battelle, LLC, under Contract No. DE-AC05-00OR22725 with the U.S. Department of Energy. The United States Government retains and the publisher, by accepting the article for publication, acknowledges that the United States Government retains a non-exclusive, paid-up, irrevocable, world-wide license to publish or reproduce the published form of this manuscript, or allow others to do so, for United States Government purposes. The Department of Energy will provide public access to these results of federally sponsored research in accordance with the DOE Public Access Plan (http://energy.gov/downloads/doe-public-access-plan).

Bottom Up Synthesis of Boron-Doped Graphene for Stable Intermediate Temperature Fuel Cell Electrodes

[#]Wesley D. Tennyson[a], [#]Mengkun Tian[b], Alexander B. Papandrew[b], Christopher M. Rouleau[a], Alexander A. Puretzky[a], Brian T. Sneed[a], Karren L. More[a], Gabriel M. Veith[c], Gerd Duscher,[c,d] Thomas A. Zawodzinski[c,d], *David B. Geohegan[a]

[a] Center for Nanophase Materials Sciences, Oak Ridge National Laboratory, Oak Ridge, TN, 37831 USA; [b] Department of Chemical and Biomolecular Engineering, University of Tennessee, Knoxville, TN 37996 USA; [c] Materials Science and Technology Division, Oak Ridge National Laboratory, Oak Ridge, TN 37831 USA; [d] Department of Materials Science and Engineering, University of Tennessee, Knoxville, TN 37996 USA

Abstract

The high surface area and electrical conductivity of few-layered graphene would make it an ideal catalyst support and electrode in fuel cells apart from its susceptibility to oxidative corrosion. Here we report the single-step, bottom-up synthesis of oxidation-resistant boron-doped graphene and show the beneficial effects of boron-doping in the aggressive electrochemical environment of intermediate temperature solid acid fuel cells (SAFCs). High yields of thin (< 20 layer) boron-doped (2-3 at.%) crystalline flakes of turbostratic graphene (B-GLF) were formed by adding boron to carbon targets that were laser vaporized under conditions identical to that for the synthesis of single wall carbon nanohorns (SWCNHs). Alternatively, adding partial pressures of hydrogen less effectively shifted the growth mode of SWCNHs toward planar, turbostratic graphene-like flakes (GLFs). Thermogravimetric analysis indicates that boron-doping enhances the oxidation resistance of few-layer GLFs by >140°C, with large fractions of multilayered B-GLFs surviving 10°C/min ramps to 1000°C. These B-GLFs provided a stable Pt catalyst support and electrode over 40 hours operation in SAFCs with cesium dihydrogen phosphate electrolyte operating at 250°C, as opposed to undoped GLFs or SWCNHs which were nearly completely consumed. The facile synthesis and oxidation-resistant properties of boron-doped GLF appear promising for graphene applications in oxidizing environments.

Keywords: CsH_2PO_4, single wall carbon nanohorns, solid acid fuel cells, few-layer graphene, boron doped carbon, boron, pulsed laser vaporization

*Corresponding authors email: geohegandb@ornl.gov

[#]Wesley D. Tennyson and Mengkun Tian contributed equally.

1. Introduction

Solid acid fuel cells (SAFCs) based on the cesium dihydrogen phosphate (CDP) electrolyte work at a medium temperature (250°C), thereby not only avoiding the materials problems associated with high temperature systems (700 to 1000°C), but offering increased catalyst activity and more useful waste heat when compared to lower temperature polymer electrolyte fuel cells (~140°C).[1-3] Additionally, SAFCs can accept a wider selection of fuels for direct oxidation, and are more resistant to CO poisoning compared to polymer electrolyte fuel cells.[4-5] However, adoption of this technology depends on further reduction of the cost of the electrodes, particularly the cathode, which typically require several mg/cm^2 of Pt. The current cathode electrode technology is based on a percolating network of Pt catalyst particles coating a macroporous ionic conductor,[6-7] wherein Pt acts as *both* the oxygen reduction catalyst and the electronic conductor. Consequently, a relatively high loading (>1.5 mg/cm^2 Pt) of Pt is needed.[6] One strategy to reduce the amount of Pt needed has been to replace the percolating network of Pt with a conductive support decorated with Pt catalysts.[8-9]

Such a support should have a large surface area to limit Pt catalyst aggregation as well as a large pore volume for fuel delivery, thus providing a high electrochemical active surface area. It should also be durable against oxidization to maintain cell activity.[10] Due to their low cost, high surface area, and ability to support small metal catalyst nanoparticles, nanostructured carbons seem ideal for SAFC electrodes. For example, carbon nanotubes have been used to increase the Pt utilization by 50x (0.014 mg/cm^2 Pt) over SAFCs based on a Pt percolating network.[11-12] Moreover, the high surface area of SWCNHs has been shown to limit catalyst coalescence during accelerated aging testing in proton exchange membrane fuel cells (PEMFC).[13] Unfortunately, as

shown in our previous work, single layer carbons are particularly vulnerable to oxidation in the SAFC environment.[9]

Multilayered graphene, for example, also satisfies these support requirements, and has a Brunauer–Emmett–Teller (BET) surface area per gram of 2600/N m^2/g that scales inversely with layer number, N.[14] This makes *few* layered graphene (less than five layers) highly attractive for high current and high durability cells, although bulk production of loose, high-quality graphene remains a challenge.[15-16] Graphene-like flakes may answer this challenge as they have been produced with high crystallinity by both arc discharge [17] and laser vaporization [18-19] into H_2/Ar gas atmospheres.

The stability of the support is particularly critical to fuel cell activity as a loss in support material can result in electrical isolation of the catalyst, thereby reducing the pore volume (fuel access), and leading to an increasing likelihood of electrocatalyst aggregation.[20] Castanheira et al., investigated the surface oxidation rate of the carbon electrode supports and found that even at low temperatures (~80°C), as in the case of PEMFC, oxidation is highly dependent on the cell potential and the defect density of the carbon support – *i.e.*, amorphous and defective materials are eroded first, even at low potentials.[21] For SAFC and PEMFC technologies, electrode support corrosion has been an ongoing problem due to the presence of high humidity.[8] With a dew point of 75°C and a cell temperature of 250°C few-layer carbon structures are particularly vulnerable to carbon corrosion (see equation 1 of cell potential (E) vs. standard hydrogen electrode (SHE)).[9]

$$\mathrm{C} + 2\mathrm{H_2O} \rightarrow \mathrm{CO_2} + 4\mathrm{H}^+ + 4\mathrm{e}^- \qquad E = 0.207V\ vs.\,\mathrm{SHE} \qquad \text{(Eq. 1)}$$

The strategies for promoting oxidation resistance have typically focused on three methods: (1) passivation of the surface to block oxygen chemisorption at specific surface active sites, (2) reduction in the number of active oxidation sites by increasing the crystalline carbon content in

the support, and (3) lowering the reactivity of the active sites by doping the carbon.[22] In the latter case, Wu *et al.*, showed that substitutional boron acts as a p-type dopant that lowers the electron density on the reactive carbon atoms, thus lowering the rate of O_2 chemisorption.[23-24] They further established the oxidation stability of boron treated graphite, and found that boron was not merely a surface passivating agent, but was unique in that it enhanced the oxidation resistance of the bulk. Further oxidation resistance may be obtained by combining these strategies, such as in the work by Lee *et al*. who produced oxidation resistant carbon fiber by using phosphorus to passivate surface sites, and boron to reduce the electron density thus lowering the reactivity of active sites.[25]

Boron has been incorporated into graphite,[26-27] carbon fiber,[28] diamond,[29] graphene,[30-33] and SWCNHs[34] by various methods including thermal post-treatments with boric acid [35] or boron oxide,[33] introduction as a co-dopant after plasma etching, such as in CBN film production,[36] or chemical vapor deposition from benzene and boron trichloride mixtures.[37] Substitutional boron in carbon can have both catalytic and inhibitive effects on carbon oxidation as shown by Radovic *et al*.[38] Specifically, the reduced electron density lowers the Fermi level and redistributes the 2p-electrons, which affects both C-O and C-C bond strengths.[38] The emerging properties of boron-doped graphene have been utilized in multiple applications from sensitive nitrogen dioxide sensors[39] to enhanced catalyst supports that limit catalyst coalescence in PEMFC.[40] In the case of SWCNHs, Harada *et al*., showed that with as little as 1 at.% boron doping, their intrinsic electrical conductivity increased nearly tenfold,[34] again underscoring the utility of boron doping in carbons.

Herein, we report advances in the single step, high yield, large scale production of oxidation-resistant boron-doped graphene-like flakes by laser vaporization synthesis for use as catalyst supports and active elements in CDP based SAFCs operating at 250°C.

2. Methods

2.1. Synthesis: pulsed laser vaporization

Carbon targets made with as-received graphite adhesive (Bay Composites BC-628) and boron-carbon targets made with graphite adhesive loaded with 9 at.% boron powder (Alfa-Aesar -325 mesh, 99% purity) were used to synthesize nanomaterials under pulsed laser vaporization (PLV) conditions employed for the synthesis of carbon nanohorns.[42] Further information on target preparation can be found in the supplemental material. The targets were mounted in a graphite holder that was inserted into a 76 mm quartz tube that was held at 1100 °C in a tube furnace (Lindberg Blue). PLV occurred in flowing Ar (2 L / min) at near atmospheric pressure (735 Torr), and the products were collected downstream in a HEPA filter.[76] The optimized laser conditions for nanohorn production utilize a Nd:YAG laser ($\lambda = 1.064$ μm) with a 20 ms pulse, 5 Hz repetition rate, and pulse energy of ~90 J focused into a 4 mm diameter spot at the target position.

Single-wall carbon nanohorns were produced with the carbon target in pure argon, and are referred to as CAr. Similarly, CH5Ar refers to nanocarbon samples produced under identical conditions except for the addition of 5% H_2 (0.1 L/min) to the 2 L/min Ar flow. Lastly, CB9Ar refers to nanocarbon samples produced in pure argon, but with the B-carbon target.

2.2. Catalyst deposition

Each of the as-synthesized materials were decorated in post treatments with platinum catalyst nanoparticles (60 wt%) that were formed by a previously reported procedure using a metalorganic $Pt(acac)_2$ precursor.[5-6, 77-78] Briefly, the powdered support materials were mixed uniformly with $Pt(acac)_2$ in a 4.5 mL glass vial in the appropriate ratios to yield 60 wt% Pt. The mixture was then heated at 210 °C under low vacuum (~600 Torr) in a N_2-H_2O atmosphere for 16 hours, causing deposition of Pt metal nanoparticles onto the support.

2.3. Cell fabrication

Solid acid fuel cells were fabricated using an anode-supported configuration, wherein sintered 304 stainless steel mesh discs (2.85 cm^2) served as the anode current collectors. This cell architecture was identical to that reported previously by others.[5-7, 77] For all cells tested, identical anodes with a Pt loading of 1.0 mg/cm^2 (Pt) were formed from a mechanical mixture of CDP, in-house synthesized 60 wt% Pt supported on carbon black (Vulcan XC-72R, Cabot Corp.), and naphthalene (a fugitive binder) in a 3:1:1 ratio, respectively, by weight. Each cell had a CDP membrane of approximately 50 μm in thickness, laminated to the anode at 125 MPa. Experimental cathodes comprised of 25 mg of a 3:1 by weight mixture of CDP and 60 wt% of Pt supported on either SWCNHs, CH5Ar, or CB9Ar were applied to the dense CDP membrane at a pressure of 30 MPa. The areal Pt loading of the experimental cathodes was 1.3 mg/cm^2.

2.4. Electrochemical testing

Cell testing was conducted using stainless steel test rigs at a temperature of 250 °C using air and ultrahigh-purity H_2, each at a dew point of 75 °C. Polarization curves were recorded (current) with a Bio-Logic VSP potentiostat by scanning the cell potential at 10 mV s^{-1} from the open circuit potential to 0 V. Each cell was subjected to a multi-step cyclic testing protocol consisting of a potentiostatic electrochemical impedance spectroscopy (EIS) spectrum at 0.8 V to obtain the average high-frequency area-specific resistance (ASR), recording of the polarization curve, a 30 minute potentiostatic hold at 0.6 V, followed by a repetition of this protocol. After 30 cycles the cells were held at 0.6 V. The ASR was used to correct the polarization curves for the effects of membrane ohmic resistance, yielding so-called iR-free polarization curves. Results presented herein were averaged across multiple cells comprising at least two replicates for each cathode formulation.

2.5. Characterization methods

Transmission electron microscopy (TEM) imaging and electron energy-loss spectroscopy (EELS) was performed in a Zeiss Libra 200MC (information limit is ~0.1 nm). The nanoparticle dimensions were estimated from the TEM micrographs using ImageJ software to trace their perimeters and calculate their cross-sectional areas. Effective nanoparticle diameters of the same areas were derived, and mean dimensions and standard deviations are reported herein. A similar procedure was used to determine flake sizes, but using a square approximation instead. EELS was used to determine the boron concentration, and background spectra were fit using a combination of a power law and a polynomial model, $E^{-r} + aE^2 + bE + c$, where a, b, c and r were fitting parameters, and E was the energy.

Scanning electron microscopy (SEM) imaging was performed with a Zeiss Auriga 40 at 3kV using the in-lens detector. BET surface area analyses were performed with a Quantachrome Micromeritics surface area and pore size analyzer. Thermogravimetric Analysis (TGA) was performed in air at a ramp rate of 10°C/min using a Q50 from TA Instruments. Lastly, X-ray diffraction (XRD) measurements were carried out on a two-circle high resolution X-ray powder diffractometer (X'Pert Pro, Panalytical) with a continuous scan using Cu-Kα_1 radiation (1.54059Å) with a fixed divergence slit of ½°.

Raman spectroscopy was performed at an excitation wavelength of 532 nm using a custom microscope-based system. A 100X objective was used to focus the laser beam on the sample with the spot size of ~1 μm, and the measured laser power at the sample location was ~0.5 mW. Note that spectral peak fitting was implemented with Lorentzian/Gaussian line shapes.

3. Results and discussion

3.1. Synthesis: Vaporization of Carbon in Ar – Sample CAr.

Laser vaporization is a method well-suited to explore the synthesis of carbon nanostructures without the use of catalysts. For example, the large scale production (kg/day) of loose and dry SWCNHs has been demonstrated with tunable morphologies ("Dahlia", "Bud", and "Seed") that are a function of laser power density.[41] Furthermore, nanostructure size can be controlled by residence time in the plume, as in the case of SWCNHs where they were observed to form with a growth rate of ~1 nm/ms of residence time in the plume.[42] Lastly, structural variations of the nanocarbons can be induced with the choice of the background gas,[43] chamber pressure,[44-45] and growth temperature.

The CAr preparation was typical of "short nanohorns,"[42] which refers to the size of an individual nanohorn unit that is typically less than 10 nm in length, and aggregates that are roughly spherical in shape with an average diameter of 60±20 nm as shown in Figure 1(a-b). Individual single-wall carbon nanohorns can be seen protruding from the aggregates as shown in Figure 1(c), and a complete list of dimensions of the materials observed in this sample can be found in Table S1 of the supplementary material.

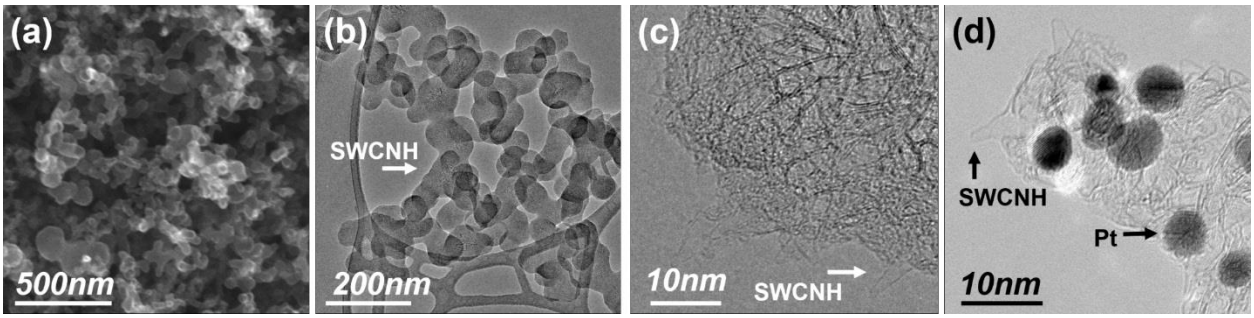

Figure 1. **Single-wall carbon nanohorns aggregates produced by pulsed laser vaporization (PLV)** (a) SEM image of the SWCNH aggregates produced by 20 msec PLV of carbon in Ar at 1100^0C, 760 Torr, and 5 Hz repetition rate. (b) TEM of the SWCNH aggregates. (c) HRTEM of protruding SWCNH from an aggregate. (d) HRTEM after deposition of Pt catalysts particles.

By combining optical and ensemble characterization techniques, the structure and uniformity of the material was determined. Micro-Raman spectra of the CAr material (Figure 2(a), upper curve) uniformly show a characteristically strong disorder-induced D-band at ~1330 cm^{-1} compared to the first-order G band at ~1585 cm^{-1}, which is indicative of the characteristically high defect density of this material.[46] Also, spectra measured from 11 random spots on this sample show that the positions of the D and G bands can vary from 1324 to 1334 cm^{-1} and from 1575 to 1593 cm^{-1}, respectively, indicating the levels of defects and graphitic character are nonuniform, at least on the length scale of the laser excitation spot (~1 μm). The results of surface area analysis using BET is shown in Table 1, and a value of ~390 m^2/g is typical of short nanohorns.[42] X-ray analysis (Figure S1) exhibited two peaks in the (002) region, and this was typical of all the samples in this work. They were well-fit by Gaussians, and the peak with lattice spacing 0.3365 nm corresponds nearly to the lattice spacing of isotropic graphite (0.3354 nm) while the one at 0.3436 nm is attributed to turbostratic carbon.[28] This splitting of the d_{002} peak was first observed in SWCNHs by Bandow *et al*., where they similarly attributed each peak to graphitic and turbostratic layered carbons.[47] Finally, Thermogravimetric Analysis (TGA) of this material (shown in Figure 2(b), blue curve and Figure S2) was characteristic of oxidizing a single phase, with a maximum derivative weight change at 590°C and ~0.1% residue remaining at 800°C, which we attribute to primarily SWCNHs and a very small fraction of graphitic material, respectively.[48]

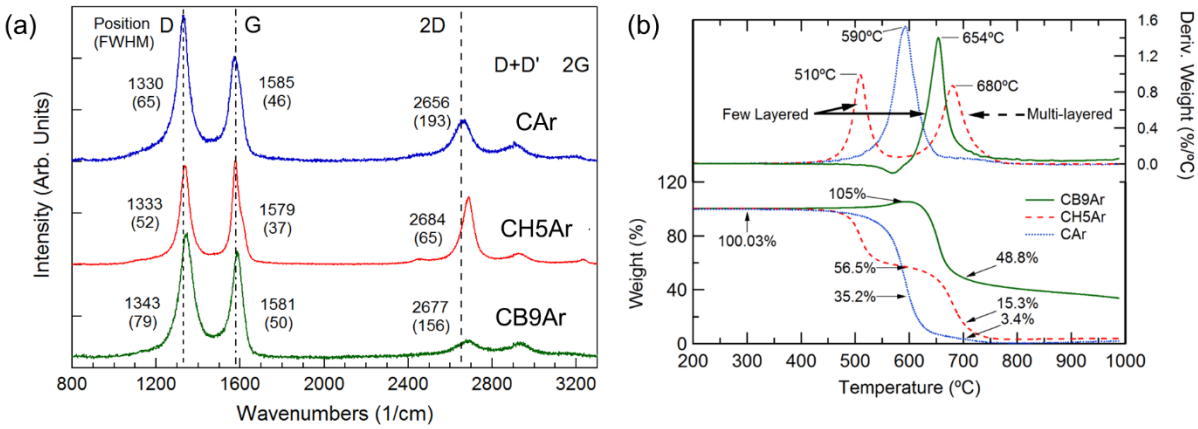

Figure 2. **Raman spectroscopy and thermogravimetric analysis of carbon nanohorns and graphene like flakes, with and without boron doping. (a)** Raman spectroscopy (λ_{ex} = 532nm) of the products from the ablation of carbon in argon, (CAr - blue), carbon in 5%H_2/Ar (CH5Ar - red), and 9%B in carbon in argon (CB9Ar - green) are shown with peak position and FWHM (in parentheses). A blue shift and broadening of the D-band was observed from the SWCNHs in CAr (1,330 cm^{-1}) to the predominately boron-doped GLF in CB9Ar (1343cm^{-1}). The G-band remains un-shifted from the pure carbon structures in CAr (1,585 cm^{-1}) and C5HAr (1579 cm^{-1}) to the boron-doped CB9Ar (1581 cm^{-1}). The 2D-band (~2660 cm^{-1}) increases with the addition of hydrogen, coincident with the formation of planar structures, and is suppressed with the addition of boron. **(b)** Thermogravimetric analysis in air with a 10^0C/min ramp rate reveals a single oxidation step for SWCNHs in CAr (blue), and two oxidation steps for CH5Ar (red) reflecting consumption of few-layered and multilayered GLFs. By comparison, the few-layered boron doped GLFs in CB9Ar (green) oxidize at 654°C with a significant fraction of multilayered GLFs surviving to 1000°C.

While the growth mechanism for single-wall carbon nanohorns has never been definitively resolved, Maruyama *et al*., studied computationally the high-temperature synthesis of fullerenes from pure carbon vapors, and showed that flat planar sp^2-bonded structures should form at ~2000°C, while curved sheets like SWCNHs that require the incorporation of sp^3 bonds necessitate higher growth temperatures (~3000°C).[49] Therefore, alteration of the laser-induced plume conditions and spatial confinement using appropriate background gases can be used to explore the synthesis of a variety of carbon nanostructures.

3.2. Synthesis: Vaporization of Carbon in 5% H_2/Ar – Sample CH5Ar

The vaporization of the carbon target into a mixture of 5% H_2 in Ar was found to shift the growth mode away from SWCNHs towards two-dimensional, layered carbon nanostructures as shown in Figure 3(a-b). TEM shows that the layered materials accompanying the SWCNHs in the sample are multilayered polyhedral graphene-like platelets (PGP, Figure 3(a) and (d)), few-layer graphene-like flakes (GLF, Figure 3(b)), and a few graphitic nanoballoons (GNB, Figure 3(b)). Accompanying this shift in growth morphology, TEM analysis reveals that the SWCNHs change as well to ones having larger individual nanohorn units (Fig. 3(c)), although the SWCNH aggregates themselves are characteristically smaller (40±11 nm) than those found in CAr (56 nm) (see Figure 3(a) and (c)).

The PGP are easily distinguished in TEM by their large size and discrete platelet shape. For example, two are shown in Figure 3(a), and a segment from the faceted perimeter is shown in Figure 3(d). In general, they are layered with an average diameter of 400±200 nm and thickness of 30±10 nm. In addition to these features, a few GNBs, similar multilayered particles with graphitic edges and hollow interiors as shown in Figure 3(b), are found with outer diameters ranging between 60 and 660 nm and wall thicknesses ranging from 6 to 60 nm. Using electron diffraction of the PGP particles, shown in Figure 3(g), we estimate the d_{002} lattice spacing to be 0.345±0.003 nm, which suggests the PGPs are rotationally faulted – *i.e.*, turbostratic. Note that this lattice spacing agrees with the d_{002} spacing of 0.3437 nm found by X-ray diffraction (XRD) (Figure S1).

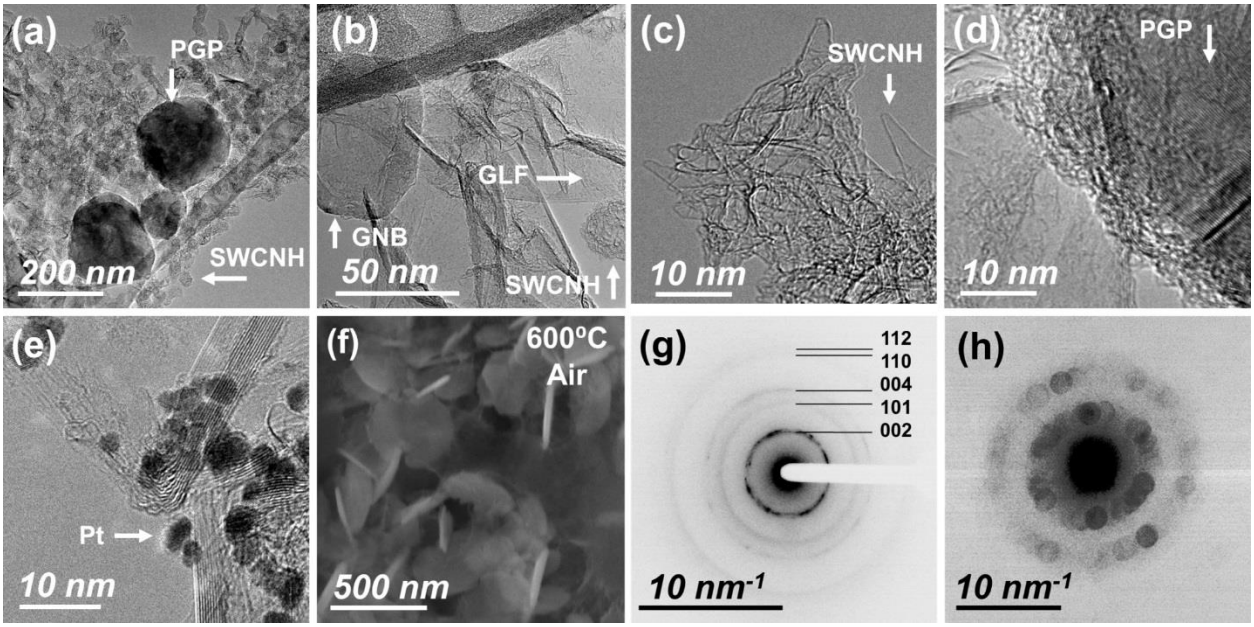

Figure 3. **Shift from SWCNHs to graphitic products in the PLV of C target with addition of 5% H_2 to Ar** (sample CH5Ar). (a) Adding 5% H_2 gas to the argon alters the laser vaporization of carbon from SWCNHs toward multilayered planar structures, which are predominantly polyhedral graphitic platelets (PGP) in roughly comparable mass fraction. (b) Lesser quantities of graphitic nano-balloons (GNB), and few-layer graphene like flakes (GLF), and SWCNHs are also found. (c) The individual SWCNH units increased in length over ablation in pure Ar. (d) Clear lattice fringes (at arrow) indicate that the PGPs are graphitic. (e) TEM of Pt-catalyst deposited on GLF prior to fuel cell testing. (f) After heating sample CH5Ar at 10C°/min to 600^0C in air by TGA, SEM image shows only discrete, thick PGP and extended, multilayered GLF remain. (g) Electron diffraction of a PGP indicates a lattice spacing of 0.345±0.003nm. (h) Nanobeam electron diffraction of an individual GLF indicates a turbostratic graphitic structure.

Quite distinct from the PGPs and GNBs are the much thinner, flexible, GLFs. The GLFs comprise less of the overall mass in the sample, but span large areas to support the other nanostructures. They consist of few-layered (less than 5 layers) to multilayered (between 5 and 20 layers) variants that are typically found together in groups of highly folded sheets, with exposed GLF-folded groups having an average diameter of 60±14 nm (Figure 3(b)). The GLFs are similarly crystalline, with a layer spacing of 0.35±0.01 nm, and are rotationally faulted as shown in the representative electron nanobeam electron diffractogram of Figure 3(h).

Raman spectra (Fig. 2a) reflect the coexistence of SWCNHs and multilayered graphene-like flakes in this sample on the length scale of the laser excitation spot (~1 μm), with the positions of the D and G bands varying from 1322 to 1344 cm^{-1} and from 1570 to 1583 cm^{-1}, respectively. However, measurements from 14 different locations in the sample indicate that 50% of the sites exhibit the characteristic spectrum of multilayer graphene as evidenced by an increase in the I_{2D}/I_G ratio (≥0.5), narrowing of the 2D band, and reduced defect density I_D/I_G ratio.

The thermogravimetric analysis of CH5Ar in Figure 2(b) (and Fig. S2) shows two clear oxidation steps at 510°C and 680°C, as well as a final residue remaining at 800°C. To help understand the relative fractions of PGP, SWCNH agglomerates, and GLFs in this sample, a fraction was heated to 600°C at the same 10°C/min rate to eliminate the easily oxidized component, and then cooled rapidly. As shown in Figure 3(f), after this controlled oxidation, the thinner-walled SWCNH and few-layered GLF observed previously were completely removed, and only PGP and some multilayered GLF remained. Based on these observations, we attribute the oxidized masses at each temperature first to the high surface area SWCNH and few-layered GLF (43.5%), and then to the intermediate surface area GLF and PGP (53.2%). The remaining 3.3% residue is attributed to the graphitic platelets. BET measurements indicated an overall reduction in surface area by over a factor of two compared to CAr, indicating an increased production of lower surface area carbons compared to SWCNHs (see Table 1). Using XRD of CH5Ar, shown in Figure S1, we estimate the graphitic fraction to be ~4% with most of the material, turbostratic, which is in good agreement with the TGA results presented earlier.

We consider two possible mechanisms that may explain why hydrogen shifts the growth conditions from SWCNH to PGP and GLF under identical vaporization conditions. In accordance with the sensitivity of the nanostructure morphology to growth temperature and confinement, it is

possible that lower growth temperatures or faster thermalization of the laser-induced plume caused by the addition of hydrogen to the Ar gas might alter the dynamics sufficiently to selectively induce planar nanostructures.[43] A second, more likely scenario is that hydrogen prevents the growth of sealed nanostructures such as nanohorns by satisfying dangling bonds at the edges of graphene sheets thus promoting the growth of planar structures. This process has been called *reactive gas induced crystallization* in arc-production of graphene.[50] These considerations may explain why large sheets of GLF are stabilized by hydrogen addition to Ar under identical vaporization conditions, however the predominant fraction of multilayered GLF and PGP formed during the short growth times provided by the ~20 ms laser pulse widths in these experiments implies either aggregation of individual sheets, or a rapid layer-by-layer growth process. The polyhedral shape of the PGPs would seem unlikely to form by aggregation, thus favoring the layer-by-layer growth mechanism.

Large platelets have been observed previously with various growth techniques. For example, Kokai *et al.* was able to form very similar PGP without hydrogen using carbon vaporization into high pressure (8 atm) Ar gas with a long pulse (500 ms) CO_2 laser, emphasizing the importance of long growth times and high temperatures.[51] Thus, the effect of hydrogen in the present study appears to be as an accelerant for assembly in the growth process, since despite the much lower Ar pressures and 20 ms laser pulses used in the present work, similar structures were obtained. Interestingly, in Kokai's study, a common precursor for the PGPs, and also the SWCNHs and folded GLFs that could also be formed, was hypothesized to be small graphene sheets. We agree with this "building block" idea, as we have reported previously that these *sheets* are found during atomic-resolution examination of the soot accompanying SWCNTs and SWCNHs formed by catalyst-assisted and catalyst-free growth, and are consistent with the theory and time-resolved

diagnostics of their growth by condensed phase intermediates.[19, 52-53] Consistent with the theory of assembly and recrystallization of single-wall graphene sheets as building blocks[54] are the results that multiwall GNBs can be produced by merely annealing fullerene soot or SWCNHs for long times in Ar at high temperature (2800^0C).[55] Thus, carbon can rapidly assemble into large microstructures without the assistance of metal catalysts (or hydrogen) in remarkably short (milliseconds) times. However, our results indicate that hydrogen can assist or alter the assembly of these graphene sheet building blocks to more easily form multilayered graphitic microstructures. This observation is supported by previous reports wherein remarkably high yields of microcones and turbostratic PGP platelets were discovered during attempts to scale up the production of carbon black using a hydrocarbon-fed plasma arc.[56] Interestingly, this process was later patented in the Kvaerner Carbon Black and Hydrogen Process[57] for the formation of primarily large microcones (termed HYCONES) that were explored as sorbents for hydrogen storage.[58]

3.3. Synthesis: Vaporization of B-Carbon in Ar – Sample CB9Ar

The addition of 9 wt.% of boron powder to the carbon target (CB9Ar) shifts the vaporization products even more completely from primarily SWCNHs towards planar structures, particularly GLFs, than with the addition of hydrogen. As estimated by surveying multiple TEM and scanning electron microscopy (SEM) micrographs, we find CB9Ar contains mostly multilayered GLFs (Figure 4(a)) and few-layered GLFs (Figure 4(b)) with average sizes of either at 100±50 nm, which is roughly three times larger in area than those made with the addition of hydrogen. However, a much smaller fraction of SWCNHs is observed, which are more defective and formed smaller aggregates (33±8 nm) (Figure 4(c)). In addition, only a few PGP (Figure S3(a)) and carbon nanotubes (Figure S3(b)) are observed, which is consistent with other reports.[59] This

shift in the production from SWCNHs to GLF is supported by a progression to still lower BET surface area (see Table 1).

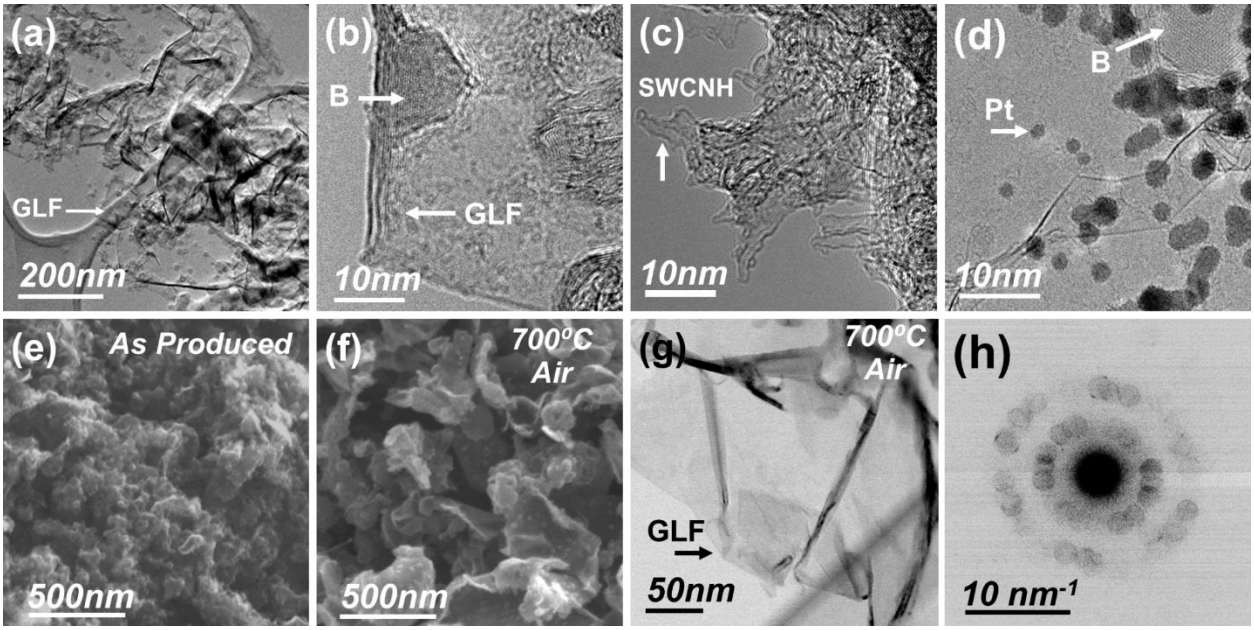

Figure 4. **Boron-doped graphene-like flakes and products from PLV of 9% B in C target in Ar.** (sample CB9Ar) (a) Low-magnification TEM shows predominately GLF, with larger flakes of few-layer GLFs supporting multilayer GLF, ~13-nm diameter B nanoparticles, and few SWCNHs. (b) Edge of a few-layer (2-4 layers) GLF and boron nanoparticle. (c) The few SWCNHs observed appeared defective, and did not form large agglomerates. (d) Pt-catalyst nanoparticles supported on few-layer GLF after chemical vapor infiltration. (e) SEM of the as-produced CB9Ar sample prior to oxidation. (f,g) SEM and TEM of sample CB9Ar after heating in air at 10C°/min up to 700^0C, effectively purifying multilayered B-doped GLF. (h) Nanobeam electron diffraction of an individual as-produced multilayered flake indicates turbostratic graphitic structure.

Table 1. Physical Properties of the Materials

	CAr	**CH5Ar**	**CB9Ar**
BET (m^2/g)	389.6	177.6	156.4
Micropore Area (m^2/g)	291.4	128.6	72.0
Raman (I_D/I_G)	1.3	0.95	1.2
Raman (I_{2D}/I_G)	0.21	0.64	0.16

Using XRD analysis we again find a splitting of the (002) peak, shown in Figure S1, with a dominant turbostratic peak and small graphitic peak (relative area ~3%). While the graphitic

peak position did not change beyond the measurement error (±0.06%), the turbostratic d_{002} spacing was reduced by 0.3%, consistent with previous reports of boron doped carbons.[28]

The presence of boron incorporated in the GLF and SWCNH was investigated using electron energy loss spectroscopy (EELS). Boron particles with average diameter of 13±3 nm decorate the GLF, as shown in Figure 4(b), but to investigate boron incorporation *within* the GLFs, regions were selected well away from the particles (see red 'x' in Figure 5(b)). Boron was consistently found with a concentration of 2-3% boron per carbon in all flakes investigated (Figure 5(a)) while boron in the SWCNHs, if present, was at a concentration below our detection limit.

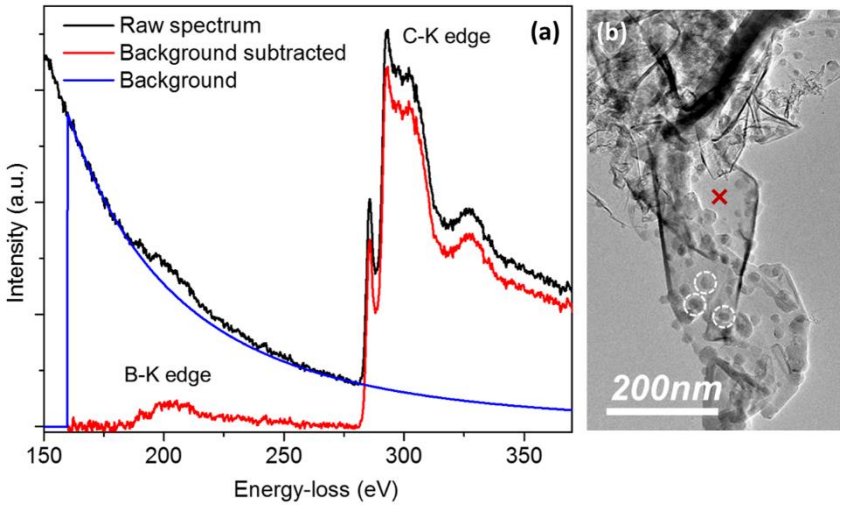

Figure 5. **Electron energy-loss spectroscopy (EELS) of the boron-doped graphene flakes.** (a) EELS areal analysis of few-layered GLF found in CB9Ar indicates 2.5±0.5% boron per carbon within the flakes. (b) EELS measurements were performed well away from the boron particles (circled in the TEM image) at positions such as that indicated by the red X.

These boron doped GLFs, or B-GLF, exhibited significantly enhanced oxidation resistance in TGA. At 750°C, for example, when the CAr and the CH5Ar sample are essentially burned out, >35% of the CB9Ar remains to 1000°C. Further analysis of the TGA data (see supplemental) shows that the thin and thick walled B-GLF materials increased in oxidation temperature over their pure carbon counterparts (CH5Ar) by ~140°C and >300°C, respectively. TEM analysis of the boron in a CB9Ar sample at 700°C reveals ~43% of the sample mass is in the form of primarily

B-GLFs (9±3 nm thick, Figure 4(g)), as well as boron doped PGPs and some carbon nanotubes (see Figure S3).

The Raman spectra of as-produced sample CB9Ar shows a significantly suppressed 2D band intensity in all 18 regions surveyed when compared to sample CH5Ar. The 2D-band suppression is consistent with other Raman spectral assessments of B-doped carbon including SWCNTs [32, 60-61], graphene[52] , and graphite[54]. We attribute the significant reduction in this band intensity to the boron doping of the GLFs, supporting our EELS observations. Furthermore, point-to-point variations were observed in the D and G bands peak positions measured in the 18 regions. The D band peak position (1343 ± 3 cm^{-1}), for example, was blue-shifted ~10 cm^{-1} compared to that of sample CH5Ar (1333 ± 7 cm^{-1}) whereas the G-band peak position was not (1581 ± 3 cm^{-1} in CB9Ar vs. 1579 ± 4 cm^{-1} in CH5Ar samples). The combination of a blue-shifted D-band and an unshifting G-band differs from that for SWCNTs, which found no significant shifts for either band. It also differs from the reported results for boron doping of graphene, which resulted in a systematic blue shift of both D and G bands[52] - *i.e.*, a D-band shifts from 1321 to 1327cm^{-1} and a G-band shifts from 1569 to 1581 cm^{-1} for 3.1 at.% boron. A possible explanation of this difference may be that in our case boron is preferentially intercalated between graphene layers instead being substitutional. This hypothesis is the subject of ongoing theoretical and experimental study.

The formation mechanism for boron-doped GLFs in our study is unclear, reflecting a longstanding mystery in similar high-temperature, non-equilibrium synthesis routes. Previous work date back to early electric arc synthesis of BN-doped MWCNTs, where some GLFs containing B without N were reported.[62] In general, boron seems to be capable of promoting graphitic structure formation by high-temperature synthesis, such as in arc or pulsed laser vaporization (PLV), but the location of individual boron atoms in the graphitic structures is

difficult to resolve.[59, 61-63] For example, by changing the plasma plume conditions from the production of primarily SWCNHs and GLFs, Kokai *et al*. reported high yield synthesis of MWCNTs (up to 60 wt.%) by continuous CO_2 laser vaporization of graphite containing boron carbide into high pressure Ar.[59] However, boron incorporation in the nanotubes could only be inferred from Raman measurements. Recently, Yuge *et al*. performed very similar experiments involving continuous CO_2 laser vaporization of carbon targets containing 2% B into atmospheric pressure Ar gas, and reported a similar mixed production of SWCNHs and GLFs.[63] There, the formation of GLFs were attributed to boron addition, and although XPS confirmed some formation of B/C bonding at ~1% levels in the sample, it was unclear whether it was the graphene-like flakes or nanohorns that contained the boron.

Our results, however, indicate that the GLFs, and not the SWCNHs, preferentially contain the boron, indicating a link between the growth mechanism of planar structures and boron doping. Compared to hydrogen's effective shift of SWCNHs formation to that of PGPs and some GLFs, it is clear that boron shifts the distribution much more effectively to larger, fewer layered GLFs. This may indicate boron's better ability to stabilize edges and prevent the termination of layers, thereby promoting the layer-by-layer growth of larger flakes. However, boron's role during synthesis is most likely related to its well-known effect as an established graphitization agent, which was extensively explored in the heat treatments of carbon fibers with boron additives at high temperatures (>2000^{0}C).[28] Boron is thought to accelerate the graphitization of carbons by virtue of its much higher self-diffusion constant in carbons (6320 cm^2/s in-plane, 8.2 cm^2/s out-of-plane) relative to carbon (82.8 cm^2/s in-plane, 1.8 cm^2/s out-of-plane).[28] Boron is also known to preferentially dope and graphitize disordered or turbostratic carbon materials over more graphitic structures. The atomistic mechanisms of the graphitization process have never been resolved, but

some first-principles calculations indicate that boron diffuses interstitially between carbon layers via a kick-out mechanism, attracting and repairing defects as it diffuses.[64] Thus, it is plausible that under the high temperature plume conditions in our experiments that boron participates during the rapid assembly of highly defective carbon nanohorns to predominantly produce more graphitic GLFs.

3.4. Electrochemical Performance in Fuel Cells

The basic kinetic relationship between potential and current can be investigated by applying potentiostatic polarization, such that the cell potential is increased at a constant rate, and the current is allowed to vary. Figure 6(a) shows polarization curves with the highest activity at 0.8 V for each of the experimental cathode materials. The CH5Ar cathode reaches 69 mA cm^{-2} at 0.8 V, while the CB9Ar and CAr cathodes attain 48 mA cm^{-2} and 60 mA cm^{-2}, respectively, at 0.8 V. In contrast to either of the other electrodes, which quickly reach maximum activity (cycle 2), the CB9Ar cathode activity evolves more slowly, peaking during the 8th testing cycle.

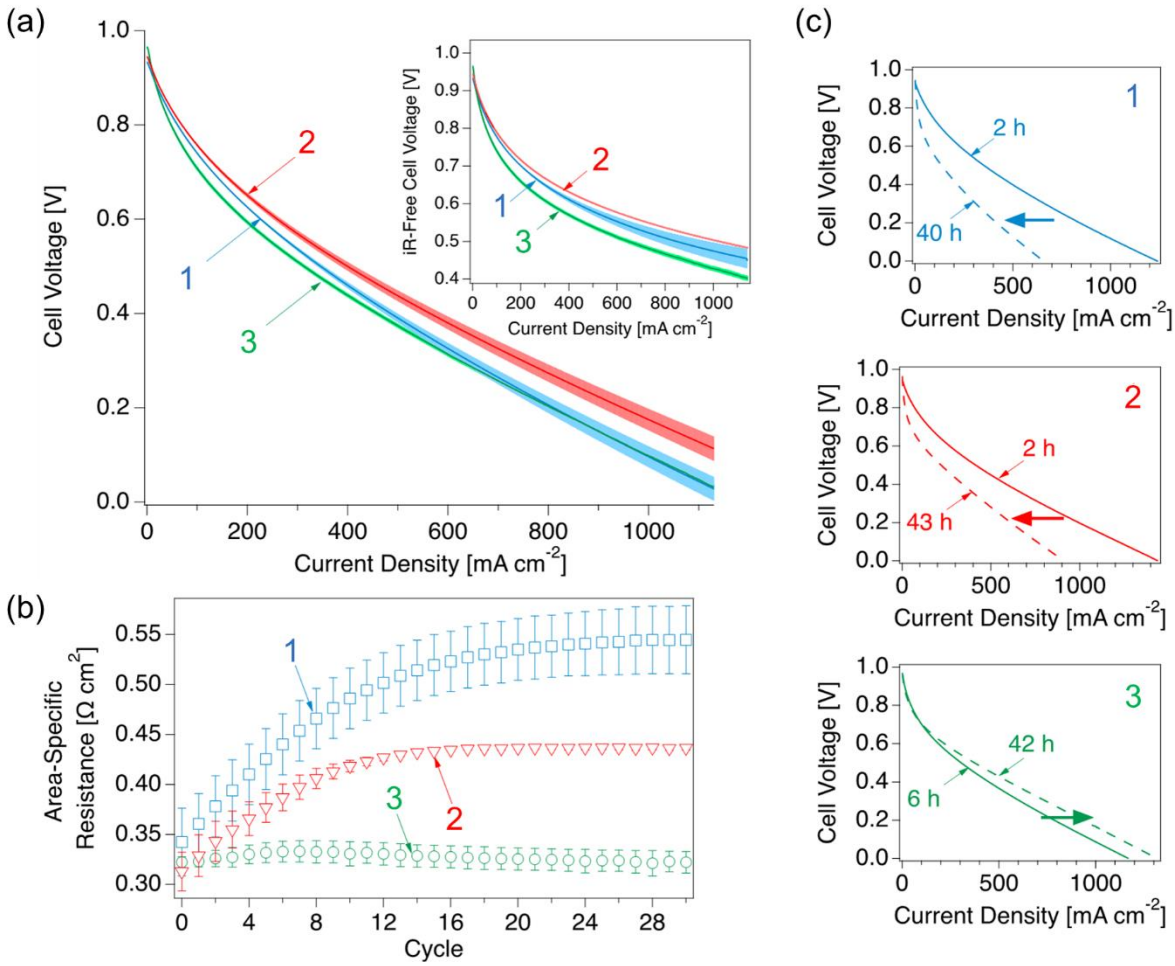

Figure 6. **Solid-acid fuel cell (CDP electrolyte, Pt catalyst) performance characteristics** recorded at 250 °C under H_2/air at 75 °C dew point with three different cathodes: (1) CAr-based, (2) CH5Ar-based, and (3) CB9Ar-based. (a) Average uncorrected polarization curves (inset shows corrected for inline resistance) where colored bands are error bars. (b) Average high-frequency area-specific resistance recorded at a cell voltage of 0.8 V. (c) Polarization curves comparing initial maximum performance (solid lines) and after ~40-hour (dashed lines).

Activity differences (current density) in SAFC cathodes can be ascribed in part to variations in the so-called tri-phase area, defined as the extent of the boundary formed by electrolyte, catalyst, and pore phases required for mutual transport of the reactants participating in the oxygen reduction reaction (ORR). The surface areas of the electrolyte and electrocatalyst, as well as the mixing of these two materials, can influence the tri-phase area. The initial current density should be proportional to the tri-phase area before electrode support degradation. Here, we note that the initial current density of the CAr cell is lower than expected compared to either

the CH5Ar or CB9Ar nanocarbons, despite it having the largest BET surface area of the three materials explored (see Table 1). The most likely explanations for this result is the CAr cell has a lower interfacial surface area from poor mixing or isolated catalysts in the solid electrolyte due to an incomplete percolation network (poor electronic contact). With regard to the observed increase of current density over time for CB9Ar, there is evidence in other work that this may be explained by either microscale flow of the plastic superionic electrolyte[12] or capillarity of the metastable liquid dehydrant phase[65-67] of CDP within the electrode acting to generate new tri-phase areas. Both observations, namely the lower than expected current density in the case of CAr and the increase of current density over time in the case of CB9Ar, indicate that the initial activity is limited primarily by the surface area of the solid electrolyte and not the support, suggesting that increases in the CDP surface area would correlate with increased cell activity.

The initially higher activity of the CAr and CH5Ar cathodes does not persist, however, and over the course of the initial 10-15 testing cycles, we observed significant changes in the cell ohmic resistance for these cathode materials (Figure 6(b)). CAr-based cathodes are affected most severely, exhibiting an increase in ohmic ASR of 58% by cycle 30. The CH5Ar cathode ASR increases by 39% over the same interval, while the ASR of the CB9Ar sample is unchanged. We attribute these results to carbon corrosion, which is a well-known degradation channel in proton-conducting electrochemical systems.[10, 21, 68-74] With water present, carbon is consumed via the reaction presented in Eq. 1, yielding gaseous carbon dioxide that is lost irreversibly. The loss of the electrode material reduces the electron pathways, increasing the ASR, and reduces the surface area of the Pt support, increasing the likelihood of catalyst ripening. The rapid increase in the ASR of the CAr electrode suggests that the SWCNHs are particularly vulnerable to carbon corrosion, and the intermediate ASR decay of the CH5Ar sample implies that the SWCNH and GLF

components of this heterogeneous support are also oxidized rapidly. This is confirmed by the post microanalysis where multilayered GLF are observed in CH5Ar, but no PGP, SWCNHs, or few-layered GLF are found (Figure 7(a, b)). The higher defect density of the SWCNH, as observed by Raman, may also contribute to their accelerated carbon corrosion (Figure 2(a)). The CB9Ar supports, on the other hand, had a surface area and defect density similar to that of CH5Ar (see Table 1). A more defective material should contribute to an increased oxidation rate by increasing the number of preferential chemisorption sites. However, in the case of the CB9Ar, we find a stable ASR that implies resistance to support corrosion. A stable ASR in boron doped materials has been previously observed in low-temperature acidic systems, and is attributed to resistance to support oxidation.[20, 70, 75] Resistance to oxidation of carbon doped with boron has been attributed to a reduced rate of O_2 chemisorption, due to a reduced electron density at the reactive carbon sites after p-type doping with boron.[24]

The initial high performance of the CAr and CH5Ar cathode cells is severely impacted by an increasing ohmic resistance over a relatively short period of ~40 hours. Figure 6(c) shows polarization curves recorded for each of the experimental cathodes at peak performance (arbitrarily determined at 0.8 V) and after approximately 40 hours of testing. We observe significant performance decay of the CAr and CH5Ar cathodes across the entire current range, despite the fact that ohmic effects tend to dominate at higher currents, since ohmic losses are linear in current density. Here we suggest two effects are occurring: first, the loss of support materials results in scission of electronic connections to catalyst sites and deactivates these sites; and second, in the absence of support materials the Pt catalysts are free to aggregate and the surface area available for ORR is lost.

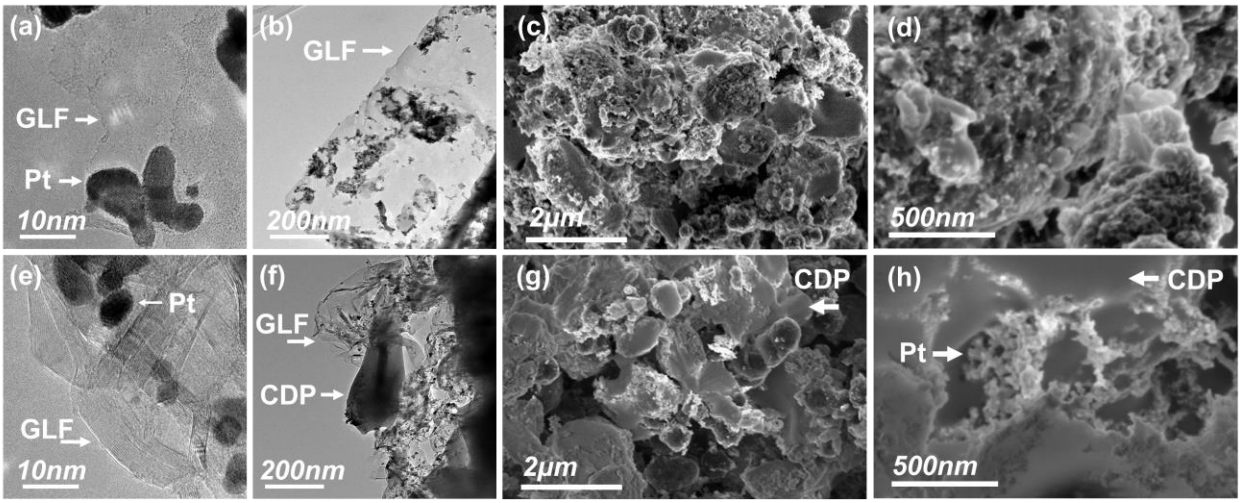

Figure 7. Post 40-hour fuel cell analysis. (a) Analysis of the CB9Ar electrode with TEM reveals few-layered B-GLF (2 to 4 layers) supporting Pt catalyst particles survive the 40-hour SAFC test. (b) Large B-GLF are found throughout the CB9Ar electrode demonstrating the material stability. (c) SEM observation of the electrode reveals that the B-GLFs remain integrally mixed with the CDP, with little exposed CDP. (d) The Pt catalyst nanoparticles remain segregated on the surfaces of the GLFs (bright spots) in the CB9Ar based electrodes. (e,f) TEM analysis of the CH5Ar cathode reveals that most carbon is consumed, with only some multilayered GLF surviving (9 to 13 layers) resulting in the exposure of large regions of solid acid electrolyte (CDP). (g) SEM analysis of the CH5Ar based electrode more clearly shows the exposed CDP electrolyte (1-2 μm diameter regions) with little conducting support. (h) The conducting networks across the CDP that remain appear to consist of agglomerated Pt catalysts.

In contrast with the large decreases in performance in the CAr and CH5Ar cells, the CB9Ar cell *increases* in performance over the course of the test at cell potentials less than 0.7 V (Figure 6(c)). These increases may arise from microstructural changes due to processes such as sintering of the CDP electrolyte in the electrode, leading to more facile proton transport. At higher voltage we do note a slight performance decay in the CB9Ar cell of ~12% at 0.8 V, which we attribute to aggregation and coalescence of Pt nanoparticles.

3.5. Cathode Characterization After Cell Operation

The absence of specific kinds of carbon structures in the electrode after fuel cell operation is direct evidence of carbon corrosion. To understand the nanomaterials responsible for the stable (CH5Ar) and increasing (CB9Ar) current density observed in the respective tests we performed a

post analysis of the cells. After 40 hours of electrochemical testing we observe that in CH5Ar only thick multilayered GLF with more than 10 layers survive as shown in Figures 7(e) and (f). No SWCNHs, few-layered GLF, or PGP are observed under TEM. Furthermore, a careful survey found very few carbon materials in the CH5Ar compared with the CB9Ar electrode. Solid electrolyte (CDP) and Pt catalyst are observed without GLF in the CH5Ar cathode, as indicated. At a larger scale, large volumes of CDP are observed decorated with Pt catalyst (bright spots) as shown in Figure 7(g). Little to no PGP or GLF can be found, indicating the carbon support had been etched away. Under higher magnification, Pt nanoparticle aggregates are observed forming an extended network, likely contributing to the electrode conductivity (see Figure 7(h)).

In contrast, the boron doped GLF in CB9Ar are readily found with few-layered GLF observed supporting Pt catalysts post fuel cell testing (Figure 7(a) and (b)). With SEM imaging, the CDP is observed coated with GLF, and appears well-connected to the electrode (minimal local charging) as shown in Figure 7(c). The catalyst Pt particles remain distributed across the GLF as observed in both TEM (Figure 7(b)) and SEM (bright spots in Figure 7(d)). The electron conduction within this sample is dominated by the remaining GLFs. However, individual Pt catalysts did coalesce (as seen in Figures 7(a) and (e)), with the average particle diameter increasing to above 6.3 nm for both samples (particle size distributions are given in Figure S4).

The GLF produced with the addition of hydrogen exhibit the typical behavior of nanostructured carbon exposed to the corrosive environment found in the SAFC, with post cell operation analysis showing that the highest surface area SWCNHs and GLF material etches away first, leaving only the thick multilayered GLF. The small residue of multilayered GLF found in the post cell operation CH5Ar electrode is likely the etched remains of layered materials with many more layers, which eventually should succumb to the oxidative environment. These results are

consistent with the residual cathode electron conductivity in the CH5Ar electrode that was found to be primarily due to the percolation network of Pt catalyst particles, suggesting that the remaining carbon was poorly connected to the electrode network, and may have avoided oxidation by electrical isolation instead of intrinsic oxidation resistance. In contrast, the CB9Ar survive through 40 hours of SAFC operation, with significant quantities of carbon found in the post analysis, and Pt catalysts observed on double layered GLF. Clearly, the boron component of the B-FLG allowed few layered materials to resist oxidation intrinsically. These results seem consistent with a reduced chemisorption rate for O_2 on a boron doped carbon as suggested by Radovic *et al*.[38]

4. Conclusions

Boron was shown to alter the growth mode of nanocarbons and simultaneously increase their electrochemical stability and oxidation resistance, enabling their use as catalyst supports and electrodes in intermediate temperature fuel cells. Adding boron to the bottom-up, laser vaporization of carbon in argon was found to very effectively shift the production of carbon nanohorns to planar, graphene like flakes with high yield (40-60 wt.%) that contained 2-4 at.% boron. The few SWCNHs found did not contain boron, indicating that boron is involved in the few-layer graphene synthesis process. Introducing hydrogen to the Ar background gas during pure carbon ablation was also found to shift the synthesis of carbon nanohorns toward planar structures that were predominantly thick, polyhedral graphitic platelets (PGPs). The uniform, faceted shape of some of these PGPs leads to the conclusion that hydrogen induces a surprisingly rapid layer-by-layer growth mode in the plume rather than gas-phase agglomeration of thinner graphene flakes.

Although the boron-doped GLF were much thinner than the PGP, they were much more robust, oxidizing during thermogravimetric measurements in air with a peak oxidation rate at 654°C

(144°C above undoped flakes), with significant fractions of multi-layered flakes surviving beyond 1000°C. Moreover, whereas all the pure carbon nanomaterials (SWCNHs, GLF, & PGPs) suffered severe carbon corrosion in the aggressive solid acid fuel cell operating conditions, the boron-doped few- and multi-layered GLFs formed surprisingly stable catalyst supports in the cathode, exhibiting a stable area specific resistance, and a current density that *increased* during fuel cell operation. Examination of these cells after 40 hours of testing revealed that the boron-doped flakes maintained a percolating conducting network with well-exposed catalyst nanoparticles. We attribute the observed increasing current density during operation to an increase in the tri-phase area resulting from either removal of the un-doped SWCNHs and other less-stable carbonaceous impurities by the aggressive oxidizing environment, and possibly microscale flow of the plastic CDP. This then results in an effective increase in the electrochemical surface area as the solid-state electrolyte becomes more able to make contact with more Pt catalyst sites. These results provide encouragement that high surface area carbons can be made much more oxidation resistant and useful as stable cathodes in aggressive SAFC environments through the addition of boron, meriting further investigation to determine the structure-functionality relationship.

AUTHOR INFORMATION

Corresponding Authors:

Email: geohegandb@ornl.gov

Author Contribution:

[#]Wesley D. Tennyson and Mengkun Tian contributed equally.

Notes

Conflict of Interest: The authors declare no competing financial interest.

Supporting Information Available: Target preparation details, images, particles dimension statistics, and additional XRD & TGA. The Supporting Information is available free of charge on the ACS Publications website

Acknowledgments
This work was supported by ARPA-E under Cooperative Agreement Number DE-AR0000499. The synthesis science was supported by the Office of Science, Basic Energy Sciences, Materials Science and Engineering Division. SWCNH and GLF synthesis, microanalysis with SEM and TEM, Raman and TGA were conducted at the Center for Nanophase Materials Sciences, which is a DOE Office of Science User Facility.

Appendix A. Supplementary data

List of Acronyms

ASR – average high-frequency Area-Specific Resistance
CDP – Cesium Dihydrogen Phosphate
EELS – Electron Energy-Loss Spectroscopy
EIS – Electrochemical Impedance Spectroscopy
GLF – Graphene Like Flake
GNP – Graphitic nano-balloon
PGP – Polyhedral Graphitic Platelet
NBED – Nanobeam Electron Diffraction
SAFC – Solid Acid Fuel Cell
SEM – Scanning Electron Microscopy
SWCNH – Single Walled Carbon Nanohorn
TEM – Transmission Electron Microscopy
TGA – Thermogravimetric Analysis
XRD – X-ray diffraction

References

1. Mahato, N.; Banerjee, A.; Gupta, A.; Omar, S.; Balani, K., Progress in material selection for solid oxide fuel cell technology: A review. *Prog. Mater. Sci.* **2015,** *72*, 141-337.
2. Haile, S. M.; Chisholm, C. R. I.; Sasaki, K.; Boysen, D. A.; Uda, T., Solid acid proton conductors: from laboratory curiosities to fuel cell electrolytes. *Faraday Discuss.* **2007,** *134* (0), 17-39.
3. Boysen, D. A.; Uda, T.; Chisholm, C. R. I.; Haile, S. M., High-Performance Solid Acid Fuel Cells Through Humidity Stabilization. *Science* **2004,** *303* (5654), 68-70.
4. Ishiyama, K.; Kosaka, F.; Shimada, I.; Oshima, Y.; Otomo, J., Glycerol electro-oxidation on a carbon-supported platinum catalyst at intermediate temperatures. *J. Power Sources* **2013,** *225*, 141-149.
5. Papandrew, A. B.; Atkinson Iii, R. W.; Unocic, R. R.; Zawodzinski, T. A., Ruthenium as a CO-tolerant hydrogen oxidation catalyst for solid acid fuel cells. *J. Mater. Chem. A* **2015,** *3* (7), 3984-3987.
6. Papandrew, A. B.; Chisholm, C. R. I.; Elgammal, R. A.; Özer, M. M.; Zecevic, S. K., Advanced Electrodes for Solid Acid Fuel Cells by Platinum Deposition on CsH2PO4. *Chem. Mater.* **2011,** *23* (7), 1659-1667.

7. Papandrew, A. B.; Chisholm, C. R. I.; Zecevic, S. K.; Veith, G. M.; Zawodzinski, T. A., Activity and Evolution of Vapor Deposited Pt-Pd Oxygen Reduction Catalysts for Solid Acid Fuel Cells. *J. Electrochem. Soc.* **2013,** *160* (2), F175-F182.
8. Sharma, S.; Pollet, B. G., Support materials for PEMFC and DMFC electrocatalysts—A review. *J. Power Sources* **2012,** *208*, 96-119.
9. Papandrew, A. B.; Elgammal, R. A.; Tian, M.; Tennyson, W. D.; Rouleau, C. M.; Puretzky, A. A.; Veith, G. M.; Geohegan, D. B.; Zawodzinski, T. A., Nanostructured carbon electrocatalyst supports for intermediate-temperature fuel cells: Single-walled versus multi-walled structures. *J. Power Sources* **2017,** *337*, 145-151.
10. Castanheira, L.; Silva, W. O.; Lima, F. H. B.; Crisci, A.; Dubau, L.; Maillard, F., Carbon Corrosion in Proton-Exchange Membrane Fuel Cells: Effect of the Carbon Structure, the Degradation Protocol, and the Gas Atmosphere. *ACS Catal.* **2015,** *5* (4), 2184-2194.
11. Thoi, V. S.; Usiskin, R. E.; Haile, S. M., Platinum-decorated carbon nanotubes for hydrogen oxidation and proton reduction in solid acid electrochemical cells. *Chem. Sci.* **2015,** *6* (2), 1570-1577.
12. Chisholm, C. R. I.; Boysen, D. A.; Papandrew, A. B.; Zecevic, S. K.; Cha, S.; Sasaki, K.; Varga, A.; Giapis, K. P.; Haile, S. M., From the Laboratory Breakthrough to Technological Realization: The Development Path for Solid Acid Fuel Cells. *Electrochem. Soc. Interface* 2009, pp 53-59.
13. Zhang, L.; Zheng, N.; Gao, A.; Zhu, C.; Wang, Z.; Wang, Y.; Shi, Z.; Liu, Y., A robust fuel cell cathode catalyst assembled with nitrogen-doped carbon nanohorn and platinum nanoclusters. *J. Power Sources* **2012,** *220*, 449-454.
14. Guo, F.; Creighton, M.; Chen, Y.; Hurt, R.; Külaots, I., Porous structures in stacked, crumpled and pillared graphene-based 3D materials. *Carbon* **2014,** *66*, 476-484.
15. Damm, C.; Nacken, T. J.; Peukert, W., Quantitative evaluation of delamination of graphite by wet media milling. *Carbon* **2015,** *81*, 284-294.
16. Yi, M.; Shen, Z., A review on mechanical exfoliation for the scalable production of graphene. *J. Mater. Chem. A* **2015,** *3* (22), 11700-11715.
17. Chen, Y.; Zhao, H.; Sheng, L.; Yu, L.; An, K.; Xu, J.; Ando, Y.; Zhao, X., Mass-production of highly-crystalline few-layer graphene sheets by arc discharge in various H2–inert gas mixtures. *Chem. Phys. Lett.* **2012,** *538*, 72-76.
18. Qian, M.; Zhou, Y. S.; Gao, Y.; Feng, T.; Sun, Z.; Jiang, L.; Lu, Y. F., Production of few-layer graphene through liquid-phase pulsed laser exfoliation of highly ordered pyrolytic graphite. *Appl. Surf. Sci.* **2012,** *258* (22), 9092-9095.
19. Geohegan, D. B.; Puretzky, A. A.; Yoon, M.; Eres, G.; Rouleau, C.; Xiao, K.; Jackson, J.; Readle, J.; Regmi, M.; Thonnard, N.; Duscher, G.; Chisholm, M.; More, K., Laser Interactions for the Synthesis and In Situ Diagnostics of Nanomaterials. In *Lasers in Materials Science*, Castillejo, M.; Ossi, P. M.; Zhigilei, L., Eds. Springer International Publishing: Cham, 2014; pp 143-173.
20. Borup, R.; Meyers, J.; Pivovar, B.; Kim, Y. S.; Mukundan, R.; Garland, N.; Myers, D.; Wilson, M.; Garzon, F.; Wood, D.; Zelenay, P.; More, K.; Stroh, K.; Zawodzinski, T.; Boncella, J.; McGrath, J. E.; Inaba, M.; Miyatake, K.; Hori, M.; Ota, K.; Ogumi, Z.; Miyata, S.; Nishikata, A.; Siroma, Z.; Uchimoto, Y.; Yasuda, K.; Kimijima, K.-i.; Iwashita, N., Scientific Aspects of Polymer Electrolyte Fuel Cell Durability and Degradation. *Chem. Rev.* **2007,** *107* (10), 3904-3951.

21. Castanheira, L.; Dubau, L.; Mermoux, M.; Berthomé, G.; Caqué, N.; Rossinot, E.; Chatenet, M.; Maillard, F., Carbon Corrosion in Proton-Exchange Membrane Fuel Cells: From Model Experiments to Real-Life Operation in Membrane Electrode Assemblies. *ACS Catal.* **2014,** *4* (7), 2258-2267.
22. Rodríguez, E.; García, R., Characterisation of boron-doped coal-derived carbon foams and their oxidation behaviour. *Fuel* **2012,** *93*, 288-297.
23. Wu, X.; Radovic, L. R., Inhibition of catalytic oxidation of carbon/carbon composites by boron-doping. *Carbon* **2005,** *43* (8), 1768-1777.
24. Yuan, B.; Xing, W.; Hu, Y.; Mu, X.; Wang, J.; Tai, Q.; Li, G.; Liu, L.; Liew, K. M.; Hu, Y., Boron/phosphorus doping for retarding the oxidation of reduced graphene oxide. *Carbon* **2016,** *101*, 152-158.
25. Lee, Y.-J.; Radovic, L. R., Oxidation inhibition effects of phosphorus and boron in different carbon fabrics. *Carbon* **2003,** *41* (10), 1987-1997.
26. Shin, H. J.; Kim, K. K.; Benayad, A.; Yoon, S. M.; Park, H. K.; Jung, I. S.; Jin, M. H.; Jeong, H. K.; Kim, J. M.; Choi, J. Y.; Lee, Y. H., Efficient Reduction of Graphite Oxide by Sodium Borohydride and Its Effect on Electrical Conductance. *Adv. Funct. Mater.* **2009,** *19* (12), 1987-1992.
27. Hagio, T.; Nakamizo, M.; Kobayashi, K., Studies on X-ray diffraction and Raman spectra of B-doped natural graphite. *Carbon* **1989,** *27* (2), 259-263.
28. Jones, L. E.; Thrower, P. A., Influence of boron on carbon fiber microstructure, physical properties, and oxidation behavior. *Carbon* **1991,** *29* (2), 251-269.
29. Polyakov, S. N.; Denisov, V. N.; Mavrin, B. N.; Kirichenko, A. N.; Kuznetsov, M. S.; Martyushov, S. Y.; Terentiev, S. A.; Blank, V. D., Formation of Boron-Carbon Nanosheets and Bilayers in Boron-Doped Diamond: Origin of Metallicity and Superconductivity. *Nanoscale Res. Lett.* **2016,** *11* (1), 1-9.
30. Jafari, A.; Ghoranneviss, M.; Salar Elahi, A., Growth and characterization of boron doped graphene by Hot Filament Chemical Vapor Deposition Technique (HFCVD). *J. Cryst. Growth* **2016,** *438*, 70-75.
31. Peng, Z.; Ye, R.; Mann, J. A.; Zakhidov, D.; Li, Y.; Smalley, P. R.; Lin, J.; Tour, J. M., Flexible Boron-Doped Laser-Induced Graphene Microsupercapacitors. *ACS Nano* **2015,** *9* (6), 5868-5875.
32. Kim, Y. A.; Fujisawa, K.; Muramatsu, H.; Hayashi, T.; Endo, M.; Fujimori, T.; Kaneko, K.; Terrones, M.; Behrends, J.; Eckmann, A.; Casiraghi, C.; Novoselov, K. S.; Saito, R.; Dresselhaus, M. S., Raman Spectroscopy of Boron-Doped Single-Layer Graphene. *ACS Nano* **2012,** *6* (7), 6293-6300.
33. Yeom, D.-Y.; Jeon, W.; Tu, N. D. K.; Yeo, S. Y.; Lee, S.-S.; Sung, B. J.; Chang, H.; Lim, J. A.; Kim, H., High-concentration boron doping of graphene nanoplatelets by simple thermal annealing and their supercapacitive properties. *Scientific Reports* **2015,** *5*, 9817.
34. Harada, M.; Inagaki, T.; Bandow, S.; Iijima, S., Effects of boron-doping and heat-treatment on the electrical resistivity of carbon nanohorn-aggregates. *Carbon* **2008,** *46* (5), 766-772.
35. Hao, Q.; Xia, X.; Lei, W.; Wang, W.; Qiu, J., Facile synthesis of sandwich-like polyaniline/boron-doped graphene nano hybrid for supercapacitors. *Carbon* **2015,** *81*, 552-563.

36. Xu, J.; Jang, S. K.; Lee, J.; Song, Y. J.; Lee, S., The Preparation of BN-Doped Atomic Layer Graphene via Plasma Treatment and Thermal Annealing. *J. Phys. Chem. C* **2014,** *118* (38), 22268-22273.
37. Way, B. M.; Dahn, J. R.; Tiedje, T.; Myrtle, K.; Kasrai, M., Preparation and characterization of Bx C(1-x) thin films with the graphite structure. *Phys. Rev. B* **1992,** *46* (3), 1697-1702.
38. Radovic, L. R.; Karra, M.; Skokova, K.; Thrower, P. A., The role of substitutional boron in carbon oxidation. *Carbon* **1998,** *36* (12), 1841-1854.
39. Lv, R.; Chen, G.; Li, Q.; McCreary, A.; Botello-Méndez, A.; Morozov, S. V.; Liang, L.; Declerck, X.; Perea-López, N.; Cullen, D. A.; Feng, S.; Elías, A. L.; Cruz-Silva, R.; Fujisawa, K.; Endo, M.; Kang, F.; Charlier, J.-C.; Meunier, V.; Pan, M.; Harutyunyan, A. R.; Novoselov, K. S.; Terrones, M., Ultrasensitive gas detection of large-area boron-doped graphene. *Proc. Natl. Acad. Sci. U. S. A.* **2015,** *112* (47), 14527-14532.
40. Yang, H. N.; Lee, D. C.; Park, K. W.; Kim, W. J., Platinum–boron doped graphene intercalated by carbon black for cathode catalyst in proton exchange membrane fuel cell. *Energy* **2015,** *89*, 500-510.
41. Azami, T.; Kasuya, D.; Yuge, R.; Yudasaka, M.; Iijima, S.; Yoshitake, T.; Kubo, Y., Large-scale production of single-wall carbon nanohorns with high purity. *J. Phys. Chem. C* **2008,** *112* (5), 1330-1334.
42. Puretzky, A. A.; Styers-Barnett, D. J.; Rouleau, C. M.; Hu, H.; Zhao, B.; Ivanov, I. N.; Geohegan, D. B., Cumulative and continuous laser vaporization synthesis of single wall carbon nanotubes and nanohorns. *Appl. Phys. A: Mater. Sci. Process.* **2008,** *93* (4), 849-855.
43. Yuge, R.; Yudasaka, M.; Toyama, K.; Yamaguchi, T.; Iijima, S.; Manako, T., Buffer gas optimization in CO2 laser ablation for structure control of single-wall carbon nanohorn aggregates. *Carbon* **2012,** *50* (5), 1925-1933.
44. Kokai, F.; Takahashi, K.; Kasuya, D.; Yudasaka, M.; Iijima, S., Growth dynamics of single-wall carbon nanotubes and nanohorn aggregates by CO2 laser vaporization at room temperature. *Appl. Surf. Sci.* **2002,** *197*, 650-655.
45. Kokai, F.; Takahashi, K.; Kasuya, D.; Nakayama, A.; Koga, Y.; Yudasaka, M.; Iijima, S., Laser vaporization synthesis of polyhedral graphite. *Appl. Phys. A* **2003,** *77* (1), 69-71.
46. Eckmann, A.; Felten, A.; Verzhbitskiy, I.; Davey, R.; Casiraghi, C., Raman study on defective graphene: Effect of the excitation energy, type, and amount of defects. *Phys. Rev. B* **2013,** *88* (3), 11.
47. Bandow, S.; Kokai, F.; Takahashi, K.; Yudasaka, M.; Qin, L. C.; Iijima, S., Interlayer spacing anomaly of single-wall carbon nanohorn aggregate. *Chem. Phys. Lett.* **2000,** *321* (5-6), 514-519.
48. Irie, M.; Nakamura, M.; Zhang, M.; Yuge, R.; Iijima, S.; Yudasaka, M., Quantification of thin graphene sheets contained in spherical aggregates of single-walled carbon nanohorns. *Chem. Phys. Lett.* **2010,** *500* (1–3), 96-99.
49. Yamaguchi, Y.; Maruyama, S., A molecular dynamics simulation of the fullerene formation process. *Chem. Phys. Lett.* **1998,** *286* (3–4), 336-342.
50. Qin, B.; Zhang, T.; Chen, H.; Ma, Y., The growth mechanism of few-layer graphene in the arc discharge process. *Carbon* **2016,** *102*, 494-498.
51. Kokai, F.; Koshio, A.; Kasuya, D.; Hirahara, K.; Takahashi, K.; Nakayama, A.; Ishihara, M.; Koga, Y.; Iijima, S., Three nanostructured graphitic particles and their growth

mechanisms from high-temperature carbon vapor confined by Ar gas. *Carbon* **2004,** *42* (12–13), 2515-2520.
52. Puretzky, A. A.; Schittenhelm, H.; Fan, X. D.; Lance, M. J.; Allard, L. F.; Geohegan, D. B., Investigations of single-wall carbon nanotube growth by time-restricted laser vaporization. *Phys. Rev. B* **2002,** *65* (24), 9.
53. Geohegan, D. B.; Schittenhelm, H.; Fan, X.; Pennycook, S. J.; Puretzky, A. A.; Guillorn, M. A.; Blom, D. A.; Joy, D. C., Condensed phase growth of single-wall carbon nanotubes from laser annealed nanoparticulates. *Appl. Phys. Lett.* **2001,** *78* (21), 3307-3309.
54. Kawai, T.; Miyamoto, Y.; Sugino, O.; Koga, Y., Nanotube and nanohorn nucleation from graphitic patches: Tight-binding molecular-dynamics simulations. *Phys. Rev. B* **2002,** *66* (3), 4.
55. Xu, G.; Niwa, H.; Imaizumi, T.; Takikawa, H.; Sakakibara, T.; Yoshikawa, K.; Kondo, A.; Itoh, S., Carbon nanoballoon produced by thermal treatment of arc soot. *New Diamond Front. Carbon Technol.* **2005,** *15* (2), 73-81.
56. Krishnan, A.; Dujardin, E.; Treacy, M. M. J.; Hugdahl, J.; Lynum, S.; Ebbesen, T. W., Graphitic cones and the nucleation of curved carbon surfaces. *Nature* **1997,** *388* (6641), 451-454.
57. Heiberg-Andersen, H.; Skjeltorp, A. T.; Sattler, K., Carbon nanocones: A variety of non-crystalline graphite. *J. Non-Cryst. Solids* **2008,** *354* (47-51), 5247-5249.
58. Gotzias, A.; Heiberg-Andersen, H.; Kainourgiakis, M.; Steriotis, T., A grand canonical Monte Carlo study of hydrogen adsorption in carbon nanohorns and nanocones at 77 K. *Carbon* **2011,** *49* (8), 2715-2724.
59. Kokai, F.; Nozaki, I.; Okada, T.; Koshio, A.; Kuzumaki, T., Efficient growth of multi-walled carbon nanotubes by continuous-wave laser vaporization of graphite containing B4C. *Carbon* **2011,** *49* (4), 1173-1181.
60. Panchokarla, L. S.; Subrahmanyam, K. S.; Saha, S. K.; Govindaraj, A.; Krishnamurthy, H. R.; Waghmare, U. V.; Rao, C. N. R., Synthesis, Structure, and Properties of Boron- and Nitrogen-Doped Graphene. *Adv. Mater.* **2009,** *21* (46), 4726-4730.
61. McGuire, K.; Gothard, N.; Gai, P. L.; Dresselhaus, M. S.; Sumanasekera, G.; Rao, A. M., Synthesis and Raman characterization of boron-doped single-walled carbon nanotubes. *Carbon* **2005,** *43* (2), 219-227.
62. Stephan, O.; Ajayan, P. M.; Colliex, C.; Ph, R.; Lambert, J. M.; Bernier, P.; Lefin, P., Doping Graphitic and Carbon Nanotube Structures with Boron and Nitrogen. *Science* **1994,** *266* (5191), 1683-1685.
63. Yuge, R.; Bandow, S.; Yudasaka, M.; Toyama, K.; Iijima, S.; Manako, T., Boron- and nitrogen-doped single-walled carbon nanohorns with graphite-like thin sheets prepared by CO2 laser ablation method. *Carbon* **2017,** *111*, 675-680.
64. Suarez-Martinez, I.; El-Barbary, A. A.; Savini, G.; Heggie, M. I., First-principles simulations of boron diffusion in graphite. *Phys. Rev. Lett.* **2007,** *98* (1), 4.
65. Taninouchi, Y.-k.; Uda, T.; Awakura, Y.; Ikeda, A.; Haile, S. M., Dehydration behavior of the superprotonic conductor CsH2PO4 at moderate temperatures: 230 to 260°C. *J. Mater. Chem.* **2007,** *17* (30), 3182-3189.
66. Taninouchi, Y.; Uda, T.; Awakura, Y., Dehydration of CsH2PO4 at temperatures higher than 260 degrees C and the ionic conductivity of liquid product. *Solid State Ionics* **2008,** *178* (31-32), 1648-1653.

67. Taninouchi, Y.-k.; Hatada, N.; Uda, T.; Awakura, Y., Phase Relationship of CsH2PO4 – CsPO3 System and Electrical Properties of CsPO3. *J. Electrochem. Soc.* **2009,** *156* (5), B572-B579.
68. Cherstiouk, O. V.; Simonov, A. N.; Moseva, N. S.; Cherepanova, S. V.; Simonov, P. A.; Zaikovskii, V. I.; Savinova, E. R., Microstructure effects on the electrochemical corrosion of carbon materials and carbon-supported Pt catalysts. *Electrochim. Acta* **2010,** *55* (28), 8453-8460.
69. Oh, H.-S.; Lee, J.-H.; Kim, H., Electrochemical carbon corrosion in high temperature proton exchange membrane fuel cells. *Int. J. Hydrogen Energy* **2012,** *37* (14), 10844-10849.
70. Antonucci, P. L.; Romeo, F.; Minutoli, M.; Alderucci, E.; Giordano, N., Electrochemical corrosion behavior of carbon black in phosphoric acid. *Carbon* **1988,** *26* (2), 197-203.
71. Roen, L. M.; Paik, C. H.; Jarvi, T. D., Electrocatalytic Corrosion of Carbon Support in PEMFC Cathodes. *Electrochem. Solid-State Lett.* **2004,** *7* (1), A19-A22.
72. Stonehart, P., Carbon substrates for phosphoric acid fuel cell cathodes. *Carbon* **1984,** *22* (4), 423-431.
73. Schmidt, T. J.; Baurmeister, J., Properties of high-temperature PEFC Celtec®-P 1000 MEAs in start/stop operation mode. *J. Power Sources* **2008,** *176* (2), 428-434.
74. Maass, S.; Finsterwalder, F.; Frank, G.; Hartmann, R.; Merten, C., Carbon support oxidation in PEM fuel cell cathodes. *J. Power Sources* **2008,** *176* (2), 444-451.
75. Acharya, C. K.; Li, W.; Liu, Z.; Kwon, G.; Heath Turner, C.; Lane, A. M.; Nikles, D.; Klein, T.; Weaver, M., Effect of boron doping in the carbon support on platinum nanoparticles and carbon corrosion. *J. Power Sources* **2009,** *192* (2), 324-329.
76. Puretzky, A. A.; Geohegan, D. B.; Fan, X.; Pennycook, S. J., Dynamics of single-wall carbon nanotube synthesis by laser vaporization. *Appl. Phys. A* **2000,** *70* (2), 153-160.
77. Papandrew, A. B.; Wilson, D. L.; M. Cantillo, N.; Hawks, S.; Atkinson, R. W.; Goenaga, G. A.; Zawodzinski, T. A., Electrochemical Hydrogen Separation via Solid Acid Membranes. *J. Electrochem. Soc.* **2014,** *161* (5), F679-F685.
78. St. John, S.; Atkinson, R. W.; Unocic, R. R.; Zawodzinski, T. A.; Papandrew, A. B., Ruthenium-Alloy Electrocatalysts with Tunable Hydrogen Oxidation Kinetics in Alkaline Electrolyte. *J. Phys. Chem. C* **2015,** *119* (24), 13481-13487.